

Optimisation of the Muon EDM measurement at the g-2 experiment



University of Liverpool, Department of Physics
George Wareing: 201634490, sggwarei@liverpool.ac.uk
Supervisor: Dr. Joe Price

This project is submitted on behalf of BSc module: PHYS379

April 29, 2025

Contents

1	Introduction	1
1.1	What is the muon?	1
1.2	How are muons produced?	1
1.3	The muon and the Standard Model	2
1.3.1	Magnetic Dipole Moment (MDM)	3
1.3.2	Electric Dipole Moment (EDM)	3
1.4	The g-2 experiment	4
1.5	Project Descriptor	5
1.6	Statistical methods that quantify an EDM	6
2	Method	8
2.1	Data Visualisation	8
2.2	Primary statistical methods	10
2.2.1	Asymmetry Λ	10
2.2.2	Average Angle $\langle \theta_L \rangle$	11
2.3	Weighted statistical methods	12
2.3.1	Initial Weighting Functions $w_{\square}, w_{\Lambda}, w_V$	12
2.3.2	Optimised Weighting Function w_S	15
3	Results	17
3.1	Primary Statistics	17
3.2	Weighted Average	17
3.3	Final Comparison	18
4	Discussion	19
4.1	The Asymmetry and Average Angle	19
4.2	The Weighted Average	20
4.2.1	Scaling the weighting function	21
4.2.2	Trialling different weighting functions	21
4.2.3	Optimising the weights	22
4.3	The overall optimisation of the EDM sensitivity	24
5	Conclusion	25

Abstract

The electric dipole moment (EDM) of the muon is a key observable that can provide insights into new physics beyond the Standard Model. This project develops a statistical framework to enhance EDM measurement sensitivity in the g-2 experiment at Fermilab. Using figure of merit (FOM) calculations, this study compares the effectiveness of primary statistics; Asymmetry Λ , and the Average Angle $\langle \theta_L \rangle$, against the Weighted Average $W(\lambda)$. Results indicate that the optimised weight w_s applied to $W(\lambda)$ improves the EDM detection across all energy decay values, with enhancements reaching up to a factor of 3.5 times compared to traditional methods. The Weighted Average consistently outperforms the conventional approach of the Asymmetry. A peak FOM = 9.9 is measured at the central positron momentum energy, reflecting a 2.3-fold enhancement compared to the conventional approach. This work establishes a robust statistical method for refining and optimising future experimental searches for the muon EDM.

1 Introduction

1.1 What is the muon?

The muon (anti-muon for this paper) is a fundamental particle in the Standard Model (SM), belonging to the lepton family. It carries an electric charge of $1.6 \times 10^{-19} C$ [1] and has a spin of $\frac{1}{2} Js$ [1], classifying it as a fermion. While it behaves similarly to the electron, the muon is 207 times more massive with a mass of $105.7 \text{ MeV}/c^2$ compared to the electron mass of $0.511 \text{ MeV}/c^2$ [1]. This characteristic results in unique interactions and a relatively short lifetime of $2.2 \mu\text{s}$ [1]. The muon was first discovered in 1936 by physicists Carl Anderson and Seth Neddermeyer while studying cosmic rays. Initially, the particle's identity puzzled researchers due to its similarities to the electron [2]. However, its discovery ultimately helped build the generational structure of the SM, differentiating the muon from the electron and laying the foundation for modern particle physics. The muon has since played a significant role in particle physics, offering insights into the behaviour of fundamental forces and particles due to its sensitivity to magnetic fields [3]. Furthermore, the muon is of particular interest due to its characteristics over the other leptons - electron and tau. The tau does not provide a sufficient lifetime to be measured by a detector, decay rapidly occurs [1]. The electron does not obtain the same sensitivity to new physics as the muon due to the differential in mass of the electron and muon. Muons are far heavier, providing sensitivity to new physics 40,000 times greater than the electron [4].

1.2 How are muons produced?

In order to produce muons, protons are accelerated to high speeds and collide with a dense target such as carbon or tungsten where they generate an array of particles as a result of the energy involved in the collision. Amongst the particles produced is the pion (π^\pm), which are particularly important due to the decay [5]:

$$\pi^+ \rightarrow \mu^+ + \nu_\mu \quad , \quad \pi^- \rightarrow \mu^- + \bar{\nu}_\mu.$$

Muons are unstable and the decay of the positive muon is through the weak interaction, decaying into a positron, electron neutrino and muon antineutrino [5].

$$\mu^+ \rightarrow e^+ + \bar{\nu}_\mu + \nu_e.$$

Figure 1 shows the Feynman diagram for muon decay, the decay of the muon is mediated through the W^+ boson, a carrier of the weak force. The decay conserves lepton flavour via the production of the $\bar{\nu}_\mu$ and ν_e balancing the decayed muon and produced positron. In weak interactions, participation is exclusive to left-handed particles and right-handed antiparticles. This leads to parity violation in muon decay, which is observable in the angular distributions of the decay products. Parity is a symmetry operation, involving the inversion of a system's spatial coordinates, akin to creating a mirror. A process is considered to be parity-conserving if it remains unchanged under such a mirror inversion. However, experiments have shown that the weak interaction (the fundamental force responsible for decay of the muon) is unique in that it violates parity symmetry [6]. This means that certain weak interaction processes look different when viewed in a mirror, an outcome that defies the usual expectations for most physical processes. This decay is mediated by the weak interaction, which is affected by the inherent asymmetry of the weak force, exclusively coupling to left-handed neutrinos and right-handed antineutrinos.

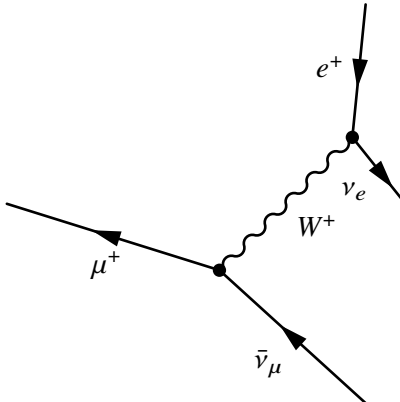


Figure 1: Feynman diagram for muon decay.

Due to the parity violating properties of the weak force, the momentum of the positron is correlated with the direction of spin of the decaying muon. Thus, the momentum of the positron can be used to study the behaviour of the spin of the muon.

1.3 The muon and the Standard Model

The SM is a theory that outlines the fundamental particles and their interactions. Excluding gravity, the SM includes three of the four recognised fundamental forces: electromagnetic, weak nuclear, and strong nuclear, with each one mediated through their corresponding gauge bosons. Within the SM, particles can be divided into two categories: fermions, which include leptons and quarks, and bosons, which serve as carriers of fundamental forces. The Higgs boson, experimentally confirmed in 2012 [7][8], provides mass to the particles via the Higgs mechanism.

While the SM has successfully explained numerous phenomena and matched experimental results, it has notable gaps, such as the absence of gravity, dark matter, and dark energy.

The intrinsic magnetism of a muon, characterised by the anomalous magnetic moment, is theoretically predicted and experimentally measured. An unexpected difference was observed when comparing these values [9]. This difference has interested physicists for decades because it could provide evidence for physics beyond the SM, potentially revealing new particles or forces that influence muons behaviour. Because of the sensitivity to a range of different physical processes, the magnetic moment of the muon and electron have played a vital role in the development of the SM.

1.3.1 Magnetic Dipole Moment (MDM)

The magnetic dipole moment (MDM) of a particle like the muon is a measure of its tendency to align its spin with an external magnetic field. It tells us about the intrinsic magnetism of the particle, for particles with spin like the muon, the magnetic moment relates to a factor, known as the gyromagnetic ratio, $\frac{gq}{2m}$. The magnetic dipole moment $\vec{\mu}$ is given [10]:

$$\vec{\mu} = g \frac{q}{2m} \vec{S}.$$

Where, $\vec{\mu}$ is the size of the MDM, and m is the mass of the particle with spin vector \vec{S} . For a simple Dirac particle with spin $\frac{1}{2}$, g should equal exactly 2 [11]. However, interactions with virtual particles slightly modify this value, leading to what is known as the anomalous magnetic moment a_μ defined as [12]:

$$a_\mu = \frac{g - 2}{2}.$$

1.3.2 Electric Dipole Moment (EDM)

The electric dipole moment (EDM) of a muon is a measure of the separation of positive and negative charge within the muon, indicating a possible violation of time-reversal (T) and CP symmetry. The electric dipole moment (EDM) \vec{d} , is given [10]:

$$\vec{d} = \eta \frac{q\hbar}{4mc} \vec{S},$$

where η represents the size of EDM, q is the particles charge and m is the particles mass. \vec{S} represents the spin vector. For muons that circulate in a storage ring, the spin vector precesses at a rate related to the magnetic dipole moments interaction with the magnetic field and the electric dipole moments interaction with the electric field. While a measurable MDM is expected, the existence of a permanent EDM in a non-degenerate quantum state remains uncertain, so the SM prediction is immeasurably small [10].

If we assume that the combined CPT symmetry, where C represents charge conjugation and P represents parity inversion, is conserved. A violation of T symmetry consequently leads to CP symmetry breaking.

However, unlike parity violation, which is maximally evident in weak leptonic processes, a violation of CP symmetry has not been observed for these leptonic processes [10].

CP violation has been experimentally confirmed in the decay of neutral kaons [13] and B-mesons [14] but this violation is at very small levels. The magnitude of such violations within the SM suggests that EDMs for leptons are exceedingly small of order $10^{-38} e\text{cm}$ [1]. As a result, the detection of these EDMs remains beyond the reach of current experimental technology. Thus, any observed non-zero EDM would be a strong indication of physics beyond the SM. The Sakharov conditions, introduced by Andrei Sakharov in 1967, are the set of criteria required to explain the observed matter-antimatter asymmetry in the universe [15]. These conditions outline the requirements for baryogenesis, the process that led to the predominance of matter over antimatter. Most notably, physical laws must violate charge conjugation symmetry (C) and combined charge-parity symmetry (CP), leading to different behaviours for matter and antimatter. The observed levels of CP violation within neutral kaons and B-mesons are insufficient to support the baryon asymmetry of the universe. Therefore, there are extra sources of CP violation that the SM does not yet describe.

1.4 The g-2 experiment

The a_μ measurement at Brookhaven National Laboratories (BNL) [10] brought to light a famous discrepancy between theoretical predictions and the measured value a_μ , resulting in the need for the Fermilab g-2 experiment. An additional measurement of the electric dipole moment \vec{d} was also made at BNL and Fermilab [10]. To do this, muons were stored in electric and magnetic fields meaning the spin is interacting with the corresponding dipole moments, \vec{d} and $\vec{\mu}$ respectively. The sum of contributions from the electric and magnetic dipole moments further relate $\vec{\omega} = \vec{\omega}_{EDM} + \vec{\omega}_{MDM}$ where [10], in the approximation $\vec{\beta} \cdot \vec{B} \approx 0$:

$$\vec{\omega}_{MDM} = -\frac{q}{m} \left[a_\mu \vec{B} + \left(-a_\mu + \frac{1}{\gamma^2 - 1} \right) \vec{\beta} \times \frac{\vec{E}}{c} \right]. \quad (1)$$

In the approximation $\vec{\beta} \cdot \vec{E} \approx 0$:

$$\vec{\omega}_{EDM} = -\eta \frac{q}{2m} \left(\vec{\beta} \times \vec{B} + \frac{\vec{E}}{c} \right) = -\frac{\eta}{2mc} \vec{F}. \quad (2)$$

q is the muon charge, \vec{B} is the main dipole field and \vec{E} is the focusing field from the electrostatic quadrupoles. **Equation 1** describes the precession of the muons magnetic moment due to the presence of both electric and magnetic fields, which arises from the anomalous magnetic moment, a_μ . The precession due to the magnetic field is related by $a_\mu \vec{B}$. The precession contribution due to the electric field, $\vec{\beta} \times \frac{\vec{E}}{c}$ where the cross product indicates that the precession depends on the direction of the velocity and electric field. The contribution of \vec{E} is minimised by setting the momentum of the muon, $\frac{1}{\gamma^2 - 1} = 1$, constricting the precession to dependency on only $a_\mu \vec{B}$.

Equation 2 describes the precession due to the EDM interactions with the cross product of the muons velocity $\vec{\beta}$ and the electric and magnetic fields. The second form of the equation rewrites the precession frequency in terms of the Lorentz force \vec{F} , the EDM directly affects the muon under the influence of both electric and magnetic fields. It is this experiment which was once done at BNL [10], that has been replicated at Fermilab [3]. In the experiment, polarised muons are circulated within a magnetic storage ring, where their magnetic moment interact with a highly uniform magnetic field. This interaction causes their spins to precess, or "wobble," at a frequency determined by the magnetic moment. The key measurement here is the difference between the frequency of the spin precession and the cyclotron frequency of the muons orbit, known as the anomalous precession frequency. This frequency difference is proportional to a_μ , allowing precise measurement of the anomaly. One of the significant implications of this setup is the potential sensitivity to effects beyond the SM. If additional particles exist that interact with the muon, they would alter its precession frequency. Notably without changing the experimental set up, measurements of the EDM were also taken. It is the gained measurement of the EDM during g-2 that this project covers.

1.5 Project Descriptor

This project aims to optimise the muon EDM measurement of the g-2 experiment at Fermilab [3]. Through statistical optimisation, an alternative framework is proposed to bring insights on the data measured at the Fermilab g-2 experiment. The initial stages of the project look at understanding the underlying probability densities of positrons from muon decay, given to me at the start of the project in the form of raw data files. Each file represents a slice of time of the muon precession period, the total precession period is split into 29 files. The structure of the files is replicated for decays generated with an EDM and without an EDM (zeroEDM), resulting in 58 total files, making direct comparison at different time slices simple. With this setup, a statistic which measures the impact of an EDM can be tested.

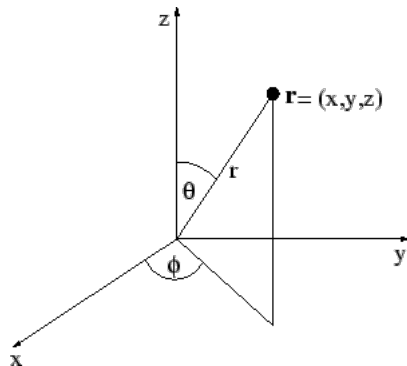


Figure 2: The coordinate system used to describe the decay positron, where ϕ is the azimuthal angle, θ is the polar angle, and r is the distance from the origin.

The data comes in the form of three parameters. The precession angle ϕ_a describes the precession due to an MDM, the full precession period is 2π . This is given as an index in the filename for both EDM and zeroEDM. A different ϕ_a represents a different point in time during the precession. The second parameter is the longitudinal (aligned with B-Field) angle of the measured positrons, θ_L . Muons decay according to **figure 1** in the storage ring and are observed in **figure 2**, at the angle θ_L , where the longitudinal angle

of decay is related to the usual polar coordinates by $\theta_L = \frac{\pi}{2} - \theta$. The angle θ_L is correlated to the tilt in the precession plane. If that average angle is zero, it is consistent with no EDM. The third parameter is the fractional energy of decayed muon λ , which ranges across a spectrum $0.2 \rightarrow 1.0$. In practice λ may also take values between $0.0 \rightarrow 0.2$ but the energy is insufficient for detection in this range.

Within each file is 500 values for the measured decay angle θ_L as the columns of data, and 500 values of the fractional energy λ as the rows. The probability density $f(\theta_L, \lambda)$ represents the number N , of muon decays at a specific λ and θ_L . For the purpose of this project, calculations use the total $\sum N$ in each file scaled to represent 1×10^5 decays. This is the structure for both EDM and zeroEDM files, but we expect larger values of θ_L for the EDM files. This data comes in the form of .pkl files.

This project requires visualising and structuring the data into a concise format. By visualising the data carefully, periodic differences introduced by the EDM will act as signatures for the EDM, and will be highlighted. The aim of this project is to develop an optimised measurement of the EDM and requires relating the corresponding EDM and zeroEDM files and calculating the difference between the average angle of decay θ_L for all λ . The difference between the files is quantified with various statistics. The best statistic is the one that gives the largest difference between EDM and zeroEDM data, taking into account the statistical uncertainties. The main aim is to provide the g-2 experiment with an optimal statistic that distinguishes between a dataset with and without an EDM.

1.6 Statistical methods that quantify an EDM

Firstly, an integral over a probability density at any given energy λ , will provide a measure of the total sum of decayed muon within each λ slice. This will be calculated by the following integral, I, where P is the probability of decay at a given fractional energy λ , and decay angle θ_L :

$$I(\lambda) = \int_{\theta_{L_{min}}}^{\theta_{L_{max}}} f(\theta_{L_i}, \lambda) \cdot d\theta_{L_i} , \quad P(\lambda) = \sum_{i=1}^{\theta_{L_i}} f(\theta_{L_i}, \lambda) \cdot \delta\theta_{L_i}. \quad (3)$$

The integral and sum form are given because in practice the probability densities are provided in a binned form. The first statistic used to quantify the effect of an EDM is the **Asymmetry**. This splits the total integral from **equation 3** in half, about $\theta_L = 0.0$, into the sum up integral N_u , and the sum down integral N_d . The metric is defined as follows:

$$\Lambda(\lambda) = \frac{N_u - N_d}{N_u + N_d}. \quad (4)$$

Where Λ denotes the Asymmetry, N_u is the $0 \rightarrow \theta_{L_{max}}$ integral and N_d is the $0 \rightarrow \theta_{L_{min}}$ integral. This numerical method to approximate the EDM has been widely used for previous analysis at Fermilab and BNL.

The second statistic is the **Average Angle** $\langle \theta_L \rangle$, this measurement is an expectation value of average θ_L , providing a measure of the central tendency of a given probability distribution. The metric is defined as follows:

$$\langle \theta_L \rangle(\lambda) = \frac{\sum_i^i f(\theta_{L_i}, \lambda) \cdot \theta_{L_i}}{\sum_i^i f(\theta_{L_i}, \lambda)}, \quad (5)$$

where i runs over the total number of θ_L bins (500).

Both the Λ and $\langle \theta_L \rangle$ statistics provide the framework to measure the EDM where the uncertainty analysis is defined for both respectively in the appendix as [12], [14]. It is the aim of the project to define the most optimal measurement of the EDM, hence the initial stages of the project compare of Λ and $\langle \theta_L \rangle$.

In the later stages, a new weighted statistical approach is proposed, using a weight $w(\theta_L, \lambda)$, applied to the **Weighted Average** $W(\lambda)$. The uncertainty on this statistic is described in the appendix [17]:

$$W(\lambda) = \frac{\sum^i w(\theta_{L_i}, \lambda) \cdot f(\theta_{L_i}, \lambda) \cdot \theta_{L_i}}{\sum^i w(\theta_{L_i}, \lambda) \cdot f(\theta_{L_i}, \lambda)}, \quad (6)$$

where i runs over the total number of θ_L bins (500). This is directly equivalent to the Average Angle $\langle \theta_L \rangle$, when $w(\theta_L, \lambda)$ is set to 1.

Each of these statistics quantifies a difference in the data due to an EDM. As a result, each must be compared equally to conclude a fair judgement of the best statistic, accounting for the uncertainties. To do this a type of χ^2 calculation is used. This can be understood through a Bayesian approach, where the prior probability is $y_i^{zeroEDM}$ and the posterior probability is y_i^{EDM} . The figure of merit (FOM), describes how well each statistical model Λ , $\langle \theta_L \rangle$, $W(\lambda)$ fits the data:

$$FOM_{\chi^2} = \sum_i^{N=29} \frac{(y_i^{EDM} - y_i^{zeroEDM})^2}{\sigma_i^{EDM^2} + \sigma_i^{zeroEDM^2}}. \quad (7)$$

Each statistic is computed over the 29 corresponding files. A bad test statistic will have no distinction between the EDM and zeroEDM data, and this will yield a zero FOM, or this may give a small distinction but with a large uncertainty. A good statistic will have a larger FOM, i.e. a large difference relative to the uncertainty. This FOM can be calculated for a slice of fractional energy λ , and hence the optimal λ can also be found. This sets the framework for testing each statistic, the most optimal statistic will yield the largest FOM value. Ultimately, this is a tool to compare the "sensitivity" of a statistic to an EDM. The final result for each statistic will appear as a table of different FOM values across λ in section [3.1, 3.2, 3.3].

2 Method

2.1 Data Visualisation

Two datasets, each comprising 29 files, were supplied, corresponding to EDM and zeroEDM for identical points in time about the muon 2π precession. EDM files had a "pseudo EDM" applied, while zeroEDM files did not, allowing for a direct comparison between datasets. This is to allow testing for each statistic, and to ultimately determine FOM values for each statistic.

To begin testing, the data must be extracted into a useful form. The structure of the .pkl files is as follows; fractional energy λ , longitudinal angle θ_L , and the precession ϕ_a , with columns of θ_L , and rows of λ . The first stages set out to visually understand the data. In **figure 3**, the data is visualised using a 2D contour plot that represents all three dimensions, revealing how the probability density changes with respect to both parameters, θ_L & λ . This is for a singular precession, $\phi_a = 0.83\pi$, there are 28 more corresponding plots that were produced. The chosen angle of precession ϕ_a is random and has no specific relevance/results above others.

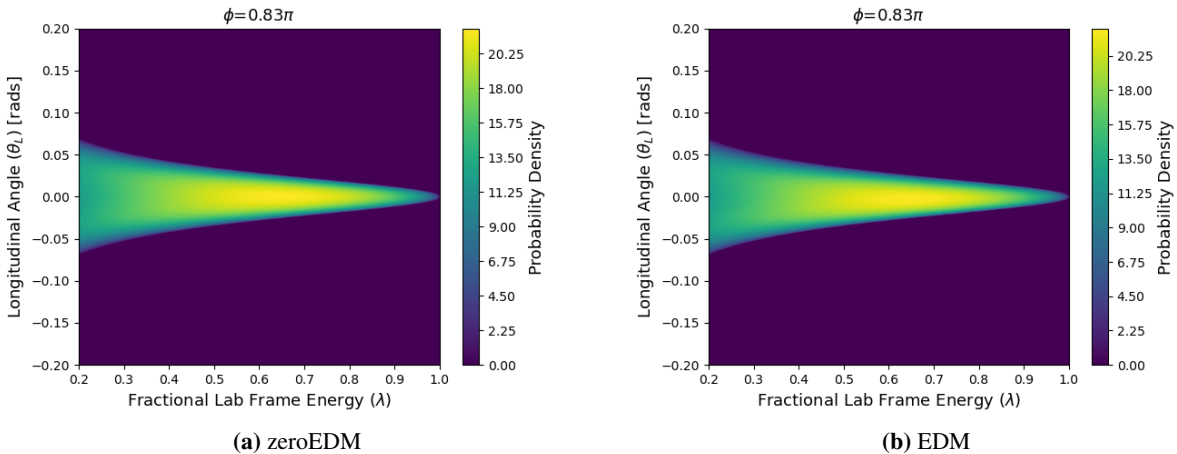


Figure 3: Comparison of probability densities. y-axis - representing the measured longitudinal angle θ_L , x-axis - Fractional Lab frame energy λ . Shown as a function of probability density $f(\theta_L, \lambda)$. For a singular precession, ϕ_a .

Figure 3 suggests that, in both the EDM and zeroEDM scenarios, the most dense probability of decay occurs in the mid-momentum positron energy, $\lambda \approx 0.5$ and central θ_L . Upon first appearance, **figure 3(a)** and **figure 3(b)** are identical; no distinct difference in θ_L is visible, however it is known that **figure 3(b)** contains the applied EDM. This set up can be broken down further to reveal impact of the tilted plane, θ_L . This is done by taking slices of probability densities $f(\theta_L, \lambda)$, dependent upon λ , allowing a more detailed look into the data to be made through the following, **figure 4**.

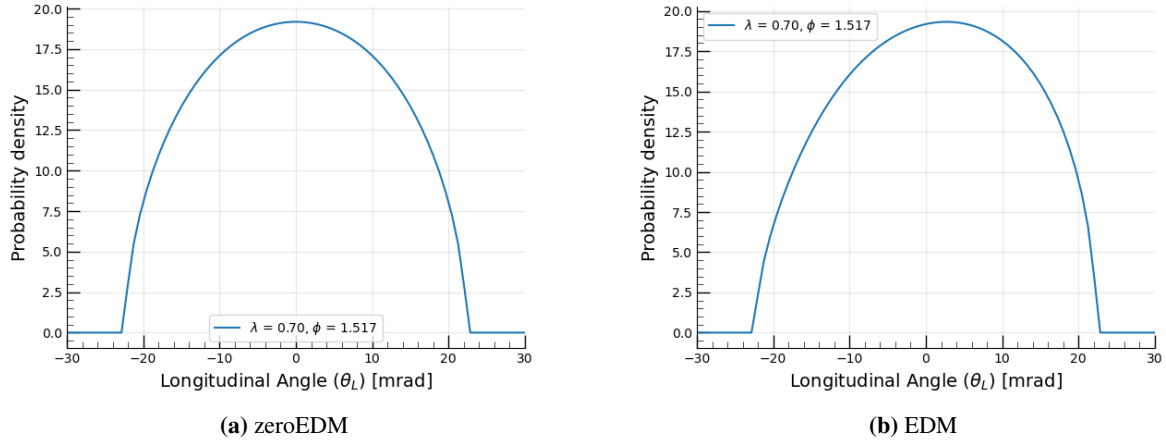
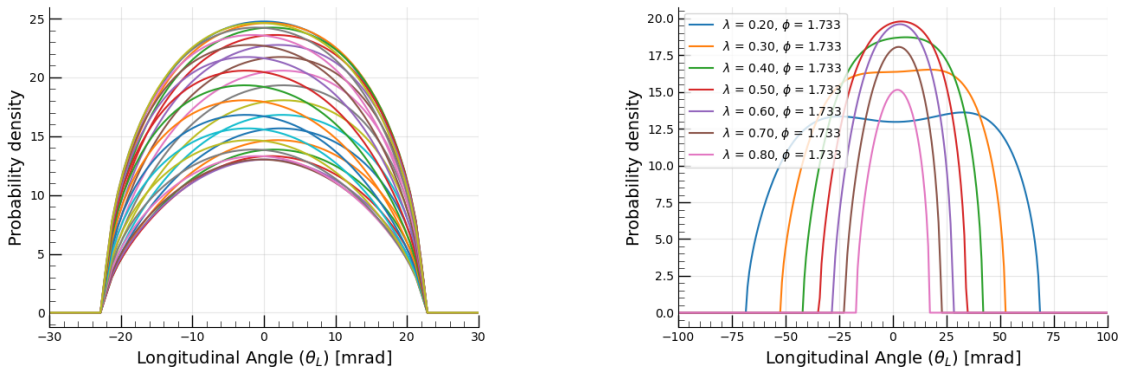


Figure 4: Comparison of singular probability densities sliced by λ . **(a)** zeroEDM and **(b)** EDM. Decay energy $\lambda = 0.7$, precession $\phi_a = 1.517\text{rads}$. There is no specific reason for the slicing to be of these values, a random choice for demonstration.

Figure 4 exhibits the marginal difference between the zeroEDM and EDM data. Visibly there is a tilt in the plane θ_L , displayed in **figure 4(b)**. This is in line with what is expected as EDM data is constructed to contain the additional component. The purpose of this breakdown is to understand how this data can be manipulated and how different parameters effect the tilt. This will allow the statistics discussed in the introduction to be applied in meaningful ways. This result of slicing the data by ϕ_a and λ reveals more about the difference between zeroEDM and EDM data than **figure 3**. Furthermore, this method was iterated across the full range of ϕ_a , at a specific energy λ . The variation that this imposes will aid in determining the most sensitive measure of EDM. This is because the probability densities are different for every ϕ_a even when λ is fixed. This is displayed in **figure 5**:



(a) Variation of ϕ_a about a full precession when keeping λ fixed at 0.7. This is specifically for EDM files, zeroEDM files are described in the appendix, **figure 17(a)**.

(b) Variation of λ across 7 different energies, but keeping ϕ_a fixed. This is for EDM files, zeroEDM files are described in the appendix, **figure 17(b)**.

Figure 5: A comparison between varying ϕ_a and λ whilst keeping each other fixed.

Figure 5(a) describes the EDM data, revealing a progressive tilt, from left to right but also scaling upwards. This is first seen in **figure 4(b)**, but now a periodic appearance is clear from **figure 5(a)**. This periodicity is key, and the project will later demonstrate how this nature provides regions of more/less sensitivity in measuring an EDM. In **figure 5(b)** we observe a variation of λ with a fixed ϕ_a , which exhibits a slight tilt toward the right due to the selection of ϕ_a . However, if ϕ_a is π out of phase, the plot would observe a tilt in the left direction. **Figure 5(b)** expresses regions of greater sensitivity from an early stage, with $\lambda \approx 0.5$ being the greatest probability density. This shows that the mid momentum energy region obtains the highest number of muon decays, and in turn could be the most sensitive region to observe an EDM.

These factors provide early insight on some of the constraints and implications for 'optimising the EDM measurement'. With this considered, the same plots are produced for zeroEDM data in **figure 17** in the appendix. **Figure 17(a)** displays no tilt when compared to the counterpart of **figure 5(a)**. Similarly, **figure 17(b)** also displays no tilt compared to the EDM counterpart, **figure 5(b)**. These results display a fraction of what can be observed through the methods described. The implications that varying λ & ϕ_a impose are used to aid the tools: Λ , $\langle\theta_L\rangle$ and $W(\lambda)$. The following stages explore how the tilt in average θ_L is quantitatively measured through the statistics discussed in section [1.6].

The aim was to maximise the efficiency of data handling through python and data structures. Firstly separation of the EDM and zeroEDM files was made through a `for` loop. Allowing iteration through the EDM and zeroEDM data separately. The following step was to store the data into a pandas data frame. Once stored in this environment the statistical measures can be tested and compared where each is defined as a function within this space, hence each phase, ϕ_a can be iterated over at any chosen energy λ , for a given statistic. Separating the statistical results by λ & ϕ_a is useful due to the specific effects each parameter has on the sensitivity of EDM detection. This also acts as space to efficiently add new functions/operations to either test or fully implement. The following statistics $\langle\theta_L\rangle$, Λ and I , were implemented into this code to initialise testing, with their uncertainties as additional functions shown in the appendix, [12], [14]. The result of this was a data frame for a specific energy λ , that contained the results due to each statistic across all 29 corresponding files with the ability to then store the data into separate EDM and zeroEDM data frames.

2.2 Primary statistical methods

2.2.1 Asymmetry Λ

We begin by measuring the Asymmetry, defined by **equation 4**. This was done by utilising the Integral tool defined by **equation 3**, a statistic to calculate both the N_u and the N_d components of the Asymmetry. The integration was performed from $0 \rightarrow \theta_{L_{max}}$ and $0 \rightarrow \theta_{L_{min}}$ using the `np.trapz` tool from the `numpy` module. This yields both N_u and N_d with associated uncertainties described in the appendix, [9], [10], [11]. The combination of results gives rise to Λ , for a single λ and ϕ_a , however this can be iterated over all ϕ_a . This was conducted for both EDM and zeroEDM data, and stored in their respective pandas data frames.

As a result the measured Λ values are visualised as a function of the precession ϕ_a . This allows for a comparison of Λ over the full precession, ϕ_a . As previously described in **figure 5(a)**, a periodic nature is prevalent within EDM files but comes in the form of an almost sinusoidal wave. Shown in **figure 6**:

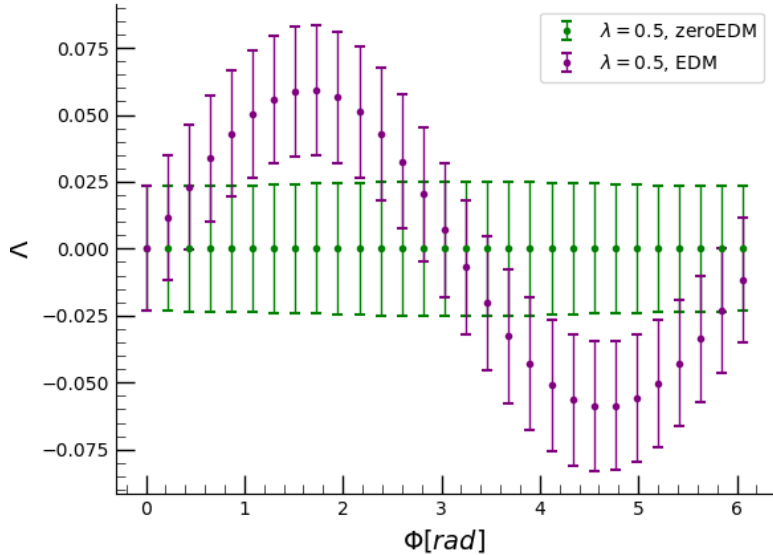


Figure 6: A full iteration of the Asymmetry statistic Λ , across the full precession ϕ_a , for a given slice of fractional energy $\lambda = 0.5$. Green corresponding to zeroEDM files and purple to EDM files. The error bars are representative of 1×10^5 decays.

Figure 6, shows the result of the statistic Λ , at a specific energy λ . First observations show that in the zeroEDM result, $\Lambda \approx 0$ across all ϕ_a . This intersects at π with the EDM values, which is the point during the precession where a tilted and untitled precession plane can't be distinguished. This indicates that the measured Asymmetry Λ , (for EDM files) is maximised at $\phi_a = \pm \frac{\pi}{2}$.

With this considered, the model at this point only observes Λ as a result of the varied ϕ_a . But the variation in the angle θ_L is also dependent upon the energy of muon decay, λ . Therefore, this was scaled in the appendix, **figure 18**, where ϕ_a and λ were varied simultaneously. The chosen energy λ , is now a range of 30 slices across $0.2 \rightarrow 0.8$. This provides a higher level overview of the statistical tool Λ as we observe it over all the parameters. Furthermore this process creates the initial framework to use the FOM calculation for the Λ statistic. We observe 30 different sets of y_{EDM} and $y_{zeroEDM}$ values for the Asymmetry, hence the ability to calculate the FOM across 30 different λ . The code to reproduce the result of the Asymmetry is described in the appendix, [28].

2.2.2 Average Angle $\langle \theta_L \rangle$

The second statistic that is used to quantify θ_L is the Average Angle, $\langle \theta_L \rangle$. The process of analysing the data follows much of the same protocol as the Asymmetry. Unlike the Asymmetry, this is not a numerical solution as there are no defined limits. Instead the statistic will compute the expectation value of average

θ_L across each probability distribution. The Average Angle is iterated over the 29 corresponding files for EDM and zeroEDM files.

The following result of the Average Angle $\langle \theta_L \rangle$, is shown in **figure 7**:

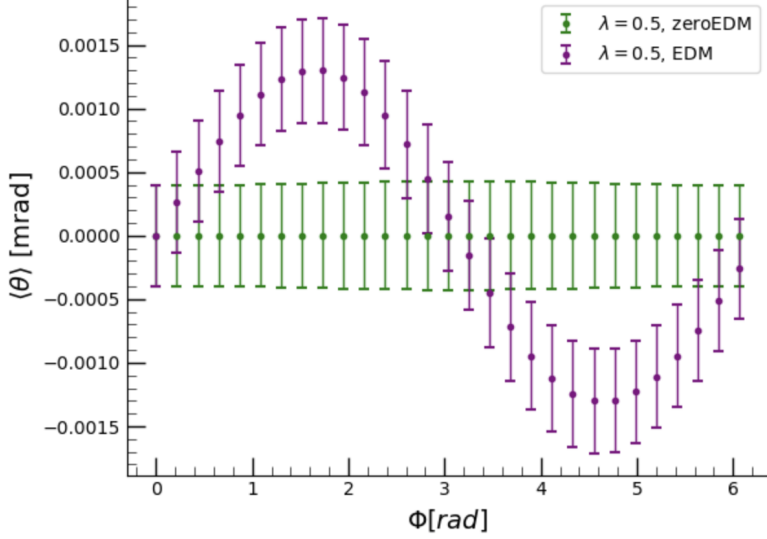


Figure 7: A full iteration of the Average Angle statistic $\langle \theta_L \rangle$, across the full precession ϕ_a for a given slice of fractional energy, $\lambda = 0.5$. Green corresponding to zeroEDM files and purple to EDM files. The error bars are representative of 1×10^5 decays.

Upon first appearance, **figures 6 & 7** are visibly similar, this highlights the importance of the FOM calculation. The first observations show that for zeroEDM data, $\langle \theta_L \rangle \approx 0$. The same sinusoidal nature is experienced for the EDM data files, with an intersection at π to zeroEDM values, which is the point during the precession where a tilted and untitled precession plane can't be distinguished. This indicates that the Average Angle $\langle \theta_L \rangle$ (for EDM files), is maximised at $\phi_a = \pm \frac{\pi}{2}$.

Similar to the Asymmetry, the model only observes $\langle \theta_L \rangle$ as a result of varying ϕ_a . But not with a variation of λ and ϕ_a simultaneously, hence this was scaled, where 30 λ slices are made across $0.2 \rightarrow 0.8$. The results for this are given in **figure 19**. The code to reproduce and implement the Average Angle, [29]. Similarly to the Asymmetry, 30 slices of λ allow the FOM to calculate 30 different results of $\langle \theta_L \rangle$. The results for Λ and $\langle \theta_L \rangle$ are compared in sections [3.1] & [4.1].

2.3 Weighted statistical methods

2.3.1 Initial Weighting Functions $w_{\square}, w_{\Lambda}, w_V$

This section explores the optimisation and statistical enhancement required to construct a more sensitive EDM detection statistic that performs better than Λ and $\langle \theta_L \rangle$. To justify this approach, it is useful to revisit the original data. When looking back at **figure 3**, the probability densities of decayed muon are a function of the decay angle θ_L and decay energy λ , for a singular ϕ_a . It was shown that the most optimal region to observe an EDM would be where the decay energy $\lambda \approx 0.5$ and for the precession, $\phi_a = \pm \frac{\pi}{2}$.

However this only provides the optimal for two parameters and does not include an optimised value of θ_L . It can be shown that the most sensitive region of detecting an EDM occurs when θ_L is at its maxima or minima, hence the final parameter θ_L can be optimised in the form of a weight on θ_L values.

From comparing **figure 5(a)** and **figure 17(a)** from the appendix, the best weighting of θ_L would occur in the higher ranges of θ_L . This is because the probability densities for zeroEDM and EDM are very similar in the central regions of θ_L . The wider ranges of θ_L describe a greater difference between the EDM and zeroEDM probability densities. With this considered, allocating a higher 'weight' to these ranges is necessary as it gives greater importance to the sensitive regions. This was done with **equation 6**, the Weighted Average $W(\lambda)$. This statistic calculates a weighted measurement of θ_L based on an allocated weight $w(\theta_L, \lambda)$. This statistic was implemented into the same code as the Asymmetry and Average Angle measurements.

This began with a basic square weight, w_{\square} set to 1.0. In theory when applied to the Weighted Average $W(\lambda)$, this would facilitate no difference to the measurement of average θ_L when compared to the Average Angle $\langle \theta_L \rangle$, as they are the same statistic in turn. The display of this weight is shown in **figure 8**:

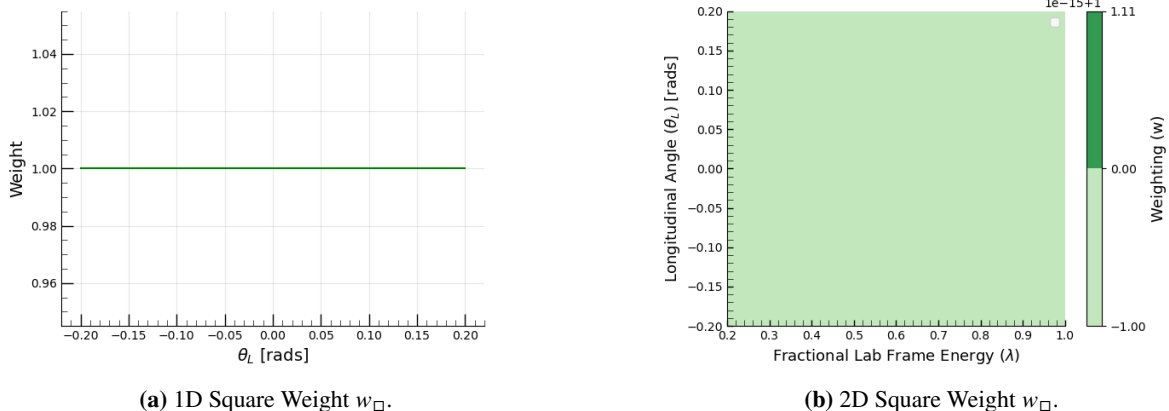


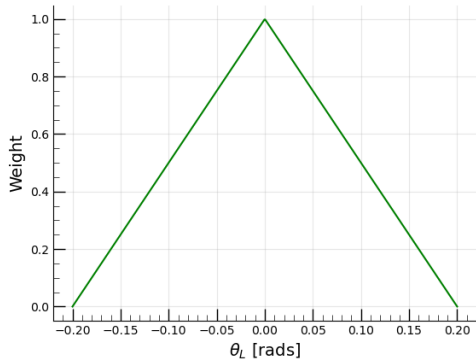
Figure 8: (a) the square weight as a function of the longitudinal angle θ_L , obtained from going 0:1 linearly from $\theta_L = -0.20 \rightarrow +0.20$. Corresponding to the ranges of the data. (b) representing the magnitude of the weight across the parameters λ and θ_L .

This correctly resulted in no change to the measurement or uncertainty. The weight w_{\square} was then scaled to a value of 400.0 to test how increasing the magnitude of a weight affects the Weighted Average. This also provided no difference to the measurement of $W(\lambda)$ and its uncertainty. This is because the weight in terms of magnitude exhibits no change, it is a linear weight that will not affect anything due to normalisation. It is rather the shape of the weight that will change $W(\lambda)$.

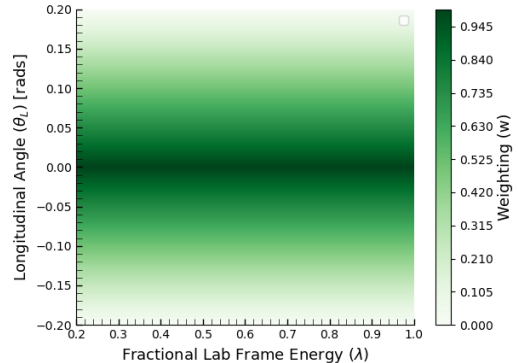
As a result, an initial weight was made that follows a triangular shape w_{Δ} . A triangular shape was chosen as the weight should be symmetric on the negative and positive θ_L values. If a continuous gradient were to be applied, it would scale incorrectly. This was constructed to experiment with how different shapes interact with the Weighted Average $W(\lambda)$.

2 Method

The following **figure 9** describes this:



(a) 1D Triangular Weight w_Λ .

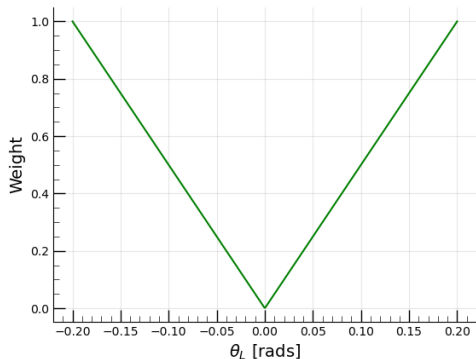


(b) 2D Triangular Weight w_Λ .

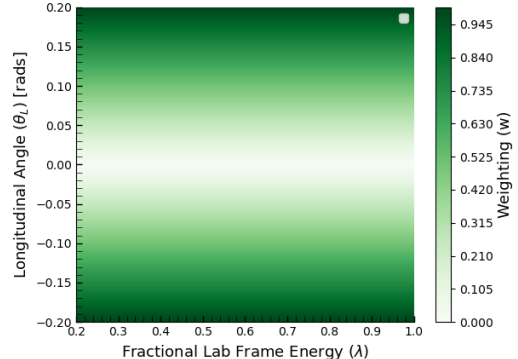
Figure 9: (a) the triangular weight as a function of the longitudinal angle θ_L , obtained by going from 0:1 linearly from $\theta_L = -0.20 \rightarrow 0$, and 1:0 from $\theta_L = 0 \rightarrow +0.20$. Corresponding to the ranges of the data. (b) representing the magnitude of the weight across the parameters λ and θ_L .

Figure 9 demonstrates how scaling the weights in a non flat shape provides an array of different weights based on θ_L and λ . It exhibits the most dense weight in the zero θ_L region, hence the weights dissipate to zero as θ_L increases and decreases to its maxima and minima. The weight is the same for all slices of decay energy λ . This creates the framework to show that changing the weight shape is what is to be optimised rather than the magnitude. However this shape does not act accordingly to the raw data and the aim of the paper. It is known that the most important regions to optimise are those with extreme θ_L , this is where we observe the changes in θ_L that are indicative of an EDM.

A third weight w_V was trialled as a result, by inverting the current shape w_Λ . This would in turn reverse the weight and place the most dense weights in the regions of extreme θ_L and smallest weights at central θ_L . This is shown in **figure 10**:



(a) 1D Inverted Weight w_V .



(b) 2D Inverted Weight w_V .

Figure 10: (a) the inverted weight as a function of the longitudinal angle θ_L , obtained from going 1:0 linearly from $\theta_L = -0.20 \rightarrow 0$ and 0:1 from $\theta_L = 0 \rightarrow +0.20$. Corresponding to the ranges of the data. (b) representing the magnitude of the weight across the parameters λ and θ_L .

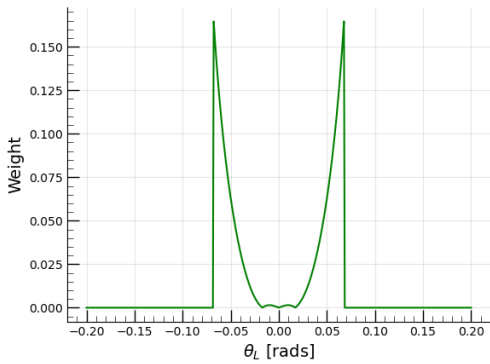
From **figure 10**, the new weighting function, w_V provides a big difference in the overall shape and density of weights. This now places the largest weight at extreme θ_L . There is now zero weight in the central θ_L region, successfully providing a better shape to describe the distribution of data from **figure 3**. This result aids the next steps in deriving the most optimal shaped weight. The key was to now shape this weight in a manner that resembles the raw data closely.

2.3.2 Optimised Weighting Function w_S

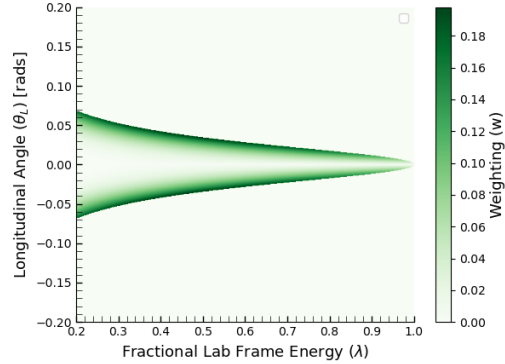
Currently the weighting functions that have been derived do not conform to the shape of the data. They provide a useful display of how different shapes affect the resultant weighting function. However they lack the ability to be different for each energy λ , angle θ_L and precession ϕ_a , hence an optimised weight, w_S must be derived from the raw data. This is a process of calculating the difference between the probability density of decayed muon between EDM and zeroEDM data.

This weight is then applied to each value of θ_L at each corresponding λ and ϕ_a , resulting in a max weight in the regions of greatest difference. In theory the best possible weighting shape, as the greatest difference in $f(\theta_L, \lambda)$ is likely to be present in the regions where θ_L sensitivity is maximal. Central θ_L values are likely to be allocated low/zero weight as they posses no difference between zeroEDM and EDM data, and hence no sensitivity.

Figure 11(b) describes the 2D contour surface of allocated weights and how it varies based on λ and θ_L . Furthermore, there will be 28 more weighted shapes similar to **figure 11(b)**, as each precession has a different result between the decay densities due to the periodic nature of this parameter, ϕ_a . Additionally each shape was then sliced by the parameter λ as shown in **figure 11(a)** because this parameter also effects decay density difference. This phenomena is referred back to **figure 5(b)** where the observed probability densities are different, when λ is varied:



(a) 1D Optimised Weight w_S .



(b) 2D Optimised Weight w_S .

Figure 11: (a) the optimised weight w_S as a function of the longitudinal angle θ_L . At precession index $\phi_a = 7$, this is for 1 singular λ slice. The shape including all 500 slices of λ for this specific ϕ_a can be found in the appendix, **figure 24**. (b) representing the magnitude of the weight across the parameters λ and θ_L for precession index (ϕ_a) = 7.

From **figure 11**, the optimised weight exhibits a largely different profile compared to the earlier weighting functions. **Figure 11(b)** displays a very distinct shape, appearing similar to the raw data shown in **figure 3**. First observations show zero weight on θ_L in regions outside of $\theta_L \approx \pm 0.07$, where there are no decays. Furthermore, the highest weights are assigned to extreme θ_L values, diminishing toward zero at the central θ_L region. This is as expected, providing a new, specific weight for each θ_L .

This method obtains specific optimised weights w_ζ , for each θ_{L_i} for a given precession ϕ_a and slice of λ . These weights were then applied to the Weighted Average, $W(\lambda)$ to compute the optimised Weighted Average across the precession ϕ_a . These results were placed into separable data frames for EDM and zeroEDM, producing results in line with the Average Angle and Asymmetry, i.e. **figures 6 & 7**. This was done not only for the optimised weight w_ζ , but all of the previous weights discussed. The results are shown in the appendix; the square weight w_\square **figure 20**, the triangular weight w_Λ **figure 21**, inverted weight w_V **figure 22** and the optimised weight w_ζ **figure 23**.

These results include all four variants of the Weighted Average $W(\lambda)$, evaluated over 30 different λ across the range $\lambda = 0.20 \rightarrow 0.80$. This enabled 30 FOM calculations on each Weighted Average, $W(\lambda)$. Additionally the code to reproduce w_ζ is attached in the appendix as [25]. The code to reproduce the standard weights $w_\square, w_\Lambda, w_V$ is included in the appendix as [26]. Furthermore the application of these weights into practice using the Weighted Average is attached in the appendix as [27]. The results for the Weighted Average $W(\lambda)$ are found in sections [3.2] & [4.2]. A final comparison between $\Lambda, \langle \theta_L \rangle, W(\lambda)$ is made in sections [3.3] & [4.3].

3 Results

This section will cover the results of both primary and weighted statistical tools that were discussed in the method, how they performed and the overall result of the best statistic at measuring the EDM. First, it is important to define how these measurements can be meaningfully compared. This returns back to the introduction where the FOM was described. This statistic will create a value of the (FOM) for any chosen energy λ . The statistic sums the difference between EDM and zeroEDM values across the full precession (this can be done for any index of precession) also receptive to the uncertainty of the measurements. A singular value of the FOM is produced for just 1 chosen energy. However this tool was implemented to access all values of λ , to give the performance of each statistic over the energy range $\lambda = 0.20 \rightarrow 0.80$. This encapsulates the measurements in the ideal way as the FOM provides exact quantitative insight in a statistics ability to classify the presence of an EDM. Larger FOM values correspond to a better measurement of the EDM.

3.1 Primary Statistics

Table 1 presents the calculated FOM values for the two primary statistics. Asymmetry and the Average Angle. The results are based on a subset of energy slices to provide an overview:

Table 1: Figure of Merit results for primary statistics, with the ratio of performance by $\langle \theta_L \rangle$ given against Λ .

Fractional Energy of Decay (λ)	$\frac{FOM_{\chi^2}}{\Lambda}$	$\frac{\langle \theta_L \rangle}{\Lambda}$
0.2	1.8	3.8
0.3	2.9	5.6
0.4	3.8	6.8
0.5	4.3	7.3
0.6	4.3	6.9
0.7	3.6	5.5
0.8	2.4	3.5

3.2 Weighted Average

This section covers the results of how the Weighted Average performed regarding the change in shape of the weighting functions $w(\theta_L, \lambda)$, discussed in the method. Similarly to the previous section, the table has a constricted number of values for the purpose of an overview.

3 Results

Table 2: Figure of Merit results for the four Weighted Average statistics $W(\lambda)$, with the ratio of the optimised weight w_S given against the original weight, w_\square .

Fractional Energy of Decay (λ)	FOM_{χ^2}				Ratio $\frac{w_S}{w_\square}$
	w_\square	w_Λ	w_V	w_S	
0.2	3.8	3.1	5.8	6.3	1.6
0.3	5.6	4.9	8.0	8.4	1.5
0.4	6.8	6.2	9.4	9.7	1.4
0.5	7.3	6.8	9.7	9.9	1.4
0.6	6.9	6.5	8.8	8.9	1.3
0.7	5.5	5.3	6.9	7.0	1.3
0.8	3.5	3.4	4.2	4.2	1.2

3.3 Final Comparison

The final table provides a comparative summary of the key statistics used to characterise an EDM, the Asymmetry and Average Angle. With the final optimised weighting function chosen due to its performance over w_\square , w_Λ and w_V .

Table 3: Figure of Merit results for Λ , $\langle \theta_L \rangle$, w_S , with the ratio of the optimised weight w_S given against the Asymmetry, Λ .

Fractional Energy of Decay (λ)	FOM_{χ^2}			Ratio $\frac{w_S}{\Lambda}$
	Λ	$\langle \theta_L \rangle$	w_S	
0.2	1.8	3.8	6.3	3.5
0.3	2.9	5.6	8.4	2.9
0.4	3.8	6.8	9.7	2.5
0.5	4.3	7.3	9.9	2.3
0.6	4.3	6.9	8.9	2.1
0.7	3.6	5.5	7.0	1.9
0.8	2.4	3.5	4.2	1.8

4 Discussion

4.1 The Asymmetry and Average Angle

An overview of the performance by the Average Angle and the Asymmetry is provided via **table 1**, demonstrating a clear difference between the two metrics. The FOM across the full energy spectrum λ , is always higher for the Average Angle when compared to the Asymmetry. Furthermore, **table 1** displays the ratio of performance of the Average Angle relative to the Asymmetry across the same energy range. **Table 1** shows that across the spectrum, the Average Angle is at least 1.5 times more effective at measuring the EDM than the Asymmetry across all energies, with the maximum ratio being 2.1 times better at $\lambda = 0.2$. **Figure 12** displays the results of the FOM across 30 different energies.

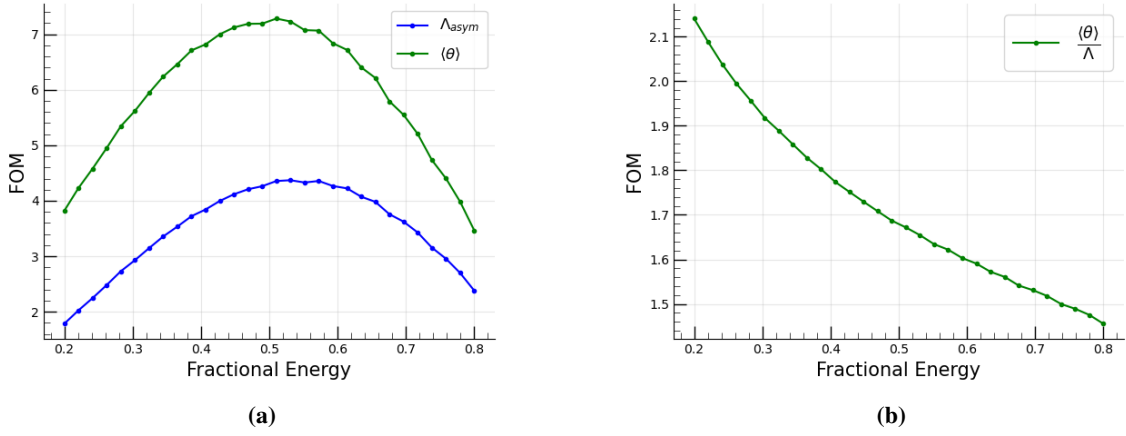


Figure 12: (a) Figure of Merit for 30 sliced energies ranging from $\lambda = 0.2 \rightarrow 0.8$. The blue line for the Average Angle and green the Asymmetry. (b) ratio of the Average Angle against the Asymmetry for 30 different energies ranging from $\lambda = 0.2 \rightarrow 0.8$.

Figure 12(a) visually displays the results of **table 1**, where the Average Angle outperforms the Asymmetry. Notably, both statistics reach their peak FOM values at $\lambda \approx 0.5$ where $\Lambda_{FOM} = 4.3$ and $\langle \theta_L \rangle_{FOM} = 7.3$.

Additionally this is a naturally occurring curved plot for both measurements, this is a fundamental property of the raw data. It is shown that in **figure 3**, the probability densities are a function of λ , where the central λ obtains the highest number of decays. **Figure 3** displays a dissipating probability of decay as λ tails either side of 0.5. This is what causes the curvature in the FOM plot. This is because each statistic is related to a counting experiment, as we are counting the number of decays, N . Therefore the uncertainty on a statistic is a function of \sqrt{N} . In the low and large λ , the number of decays decrease, hence we observe fewer N in these regions. This decrease in N decays forms larger uncertainties on the low and large λ values of any statistic. Therefore at low and large λ the FOM decreases as σ^{EDM} and $\sigma^{zeroEDM}$ are both larger relative to the measurement. This is the core reason for the curvature, and is carried forward through all statistical measures as this is a counting experiment.

Figure 12(b) shows a curved decrease in the ratio of Average Angle to the Asymmetry. **Table 1** shows the greatest ratio of 2.1 occurs at $\lambda \approx 0.2$. The lowest value of their ratio, 1.5 occurs at $\lambda \approx 0.8$. This is related back to **figure 3**. When taking slices of λ from **figure 3**, the largest width of decay angles θ_L , occur at the low λ and this slowly dissipates as λ increases to 1.0. The Average Angle can encapsulate more of the data as it does not depend on two summed integrals, therefore it provides more sensitivity to wider θ_L values compared to the Asymmetry. This means that as we observe λ increasing, the width of θ_L decreases, hence the advantage that the Average Angle provides over the Asymmetry worsens, causing the decline in the ratio.

The Average Angle, generally performs better as a statistical measure compared to the Asymmetry, because it directly incorporates all available data points rather than just a split sum over two regions. The Asymmetry only considers the total counts in each half of the distribution, reducing all available information to just two numbers: N_d and N_u . It is worth noting that the Asymmetry does not make measurements of the angle θ_L , rather just the number up and the number down. This statistic was used at BNL, where the detectors do not encompass the measured angle rather just a counting experiment for decayed muon into two separate detectors. In contrast, at Fermilab the detectors are able to measure this angle θ_L precisely. This leads to the Average Angle accounting for the entire shape of the distribution, weighted by the values of $f(\theta_L, \lambda)$, making it more robust. Moreover, Asymmetry is highly sensitive to binning and the choice of integration limits, whereas the Average Angle smoothly integrates all contributions, reducing the impact of binning.

Additionally, the uncertainty in Asymmetry, means that it suffers from high variance, especially when counts are low. The Asymmetry will always result in marginally larger uncertainty, a biased estimator. In contrast, the standard uncertainty of the Average Angle is Bessel corrected, providing an estimator that is unbiased. Finally, if the distribution is nearly symmetric, Asymmetry approaches zero, making small deviations difficult to detect, whereas the Average Angle remains sensitive to even minor shifts. Therefore, the Average Angle serves as a more continuous, smooth, and precise measure compared to Asymmetry, which is often noisier and less informative.

The results from **table 1** act as an initial benchmark for measuring the EDM, where the previous limit of detection, $\Lambda_{FOM} = 4.3$ is outperformed by $\langle \theta_L \rangle_{FOM} = 7.3$. This new limit of detection is now compared in section [4.2] against the Weighted Average $W(\lambda)$ and the four weighting functions described in section [2.3].

4.2 The Weighted Average

The concept of the Weighted Average arises from the understanding of the Average Angle. Early results suggested the Average Angle outperforms the Asymmetry, hence it was deduced there will be some idealised weighting function that provides a better statistic than the Average Angle (**equation 5**), which comes in the form of the Weighted Average, (**equation 6**). This means that when a weight of 1.0 is applied to $W(\lambda)$, the result is $\langle \theta_L \rangle$.

The raw data represents signal events, where the probability density $f(\theta_L, \lambda)$ is a bin of events characterised by the energy spectrum λ and the measured angle, θ_L . In theory an idealised weight would provide

greater emphasis to the data which are deemed most sensitive to an EDM. As previously discussed the most probable regions of EDM detection are the more extreme θ_L values. In practice the raw data will not arrive in the form of two different points in time, one with an EDM and one with zeroEDM. It will be one singular file, it is the purpose of this project to determine a statistic that provides the most confidence when measuring EDM data. Furthermore, the placement of higher weights in the extreme θ_L regions means the new detection of an EDM will be more sensitive to an EDM measurement. This means fewer events are required to determine whether an EDM is actually present in the data, making it a more efficient analysis.

4.2.1 Scaling the weighting function

Weighting the events is not the same as increasing the number of decays. As such, scaling all the weights by the same factor should not affect the Weighted Average. As discussed in the method, an initial weight w_{\square} was constructed shown in **figure 8**, this weight was set to 1.0, which is assumed to make no difference to the Weighted Average when compared to the Average Angle. The result of this is in line with what is expected, shown by the values in **table 2**, where the measured FOM is identical to the Average Angle from **table 1**. The results; $\langle \theta_L \rangle_{FOM} = 7.3$ and $W(w_{\square})_{FOM} = 7.3$ at $\lambda \approx 0.5$, proving that the initial weight is successful.

Furthermore, w_{\square} was then scaled to 400, an arbitrary constant higher than 1.0. This also results in no difference in the Weighted Average compared to when the weights were all set to $w = 1.0$. This sanity check confirms that the weight, and the Weighted Average, are being calculated correctly.

4.2.2 Trialling different weighting functions

Since scaling the applied weight is demonstrated to not affect the Weighted Average, or the FOM, to deduce a better weighting function it would need to change the shape of the applied weight. This began with **figure 9(a)**, where an initial shape change was made into a triangular shape to give a new weight, w_{Δ} . From **table 2**, this change from w_{\square} to w_{Δ} performs worse than the current limit of the Average Angle across all λ . A peak value is determined as $W(w_{\Delta})_{FOM} = 6.8$ occurring at $\lambda \approx 0.5$. This is because the largest weights are placed in the central region of θ_L , which implies the Weighted Average calculation places a higher sensitivity on central θ_L shown in **figure 9(b)**. This means that the extreme θ_L values have smaller weights relative to the centre and in turn, there is a larger uncertainty on the important values of θ_L . This causes a decreased FOM across the spectrum λ shown in **table 2**.

This led to the deduction of the third weighting shape w_V . It was assumed with a lower performing Weighted Average due to w_{Δ} , that inverting this would in turn, do the opposite and provide a better FOM. The inverted weight **figure 10(a)** displays the greatest weights being placed in a linear shape from a maximum of $\pm\theta_L$ down to 0. Which implies a zero weight at the central region. This also means the uncertainty on sensitive regions of θ_L is now smaller compared to the all previous statistics and weighted functions. The results of this, a Weighted Average that is more precise and sensitive to an EDM.

From **table 2** it is shown that the FOM for the Weighted Average is better when using w_V , compared to w_\square and w_Λ . This occurs across the full spectrum with a peak value of $W(w_V)_{FOM} = 9.7$ occurring at $\lambda \approx 0.5$. Therefore a new limit of detection is made, beating the previous limit of the Average Angle.

This result clarifies that weighting extreme θ_L regions provides greater sensitivity to measuring an EDM. With the Weighted Average now placing higher weights to the extreme θ_L , when the calculation of the FOM is made for each λ value, the difference between zeroEDM ($y_i^{zeroEDM}$) and EDM values (y_i^{EDM}) is greater than before as the uncertainty of the Weighted Average is smaller in comparison to weights, w_\square and w_Λ . N is larger in the sensitive regions, therefore this increases \sqrt{N} , which further reduces the uncertainty σ_w . This reason gives rise to the larger FOM and new detection limit above the Average Angle. Whilst this shape, w_V acting on $W(\lambda)$ provides a new limit above the Average Angle and Asymmetry. The shape does not conform to the idealised shape. This is because the weighting is still not optimised based on the parameters $\lambda, \theta_L, \phi_a$.

4.2.3 Optimising the weights

The introduction of shape 4, w_S , marks it as the most optimal shape. The observations revert to **figure 3**. The variation in probability density does not seem significantly different between **figure 3(a)** and **figure 3(b)**. Nevertheless, when λ is sliced, the EDM probability densities compared to the zeroEDM probability densities reveal a marked difference. In the zeroEDM **figure 17(a)**, the probability densities remain aligned without tilt, whereas the EDM probability densities in **figure 5(a)** exhibit a central tilt. This additional tilted zone in the EDM plots signifies an EDM presence.

An optimised weight w_S was designed to assess the difference between the probability densities of EDM and zeroEDM. This function delivers precise quantitative insight into the discrepancy between these probability distributions. Any significant surplus of this difference indicates an EDM signal. It provides an optimal weighting function, assigning minimal weight to the central θ_L regions where probability densities for EDM and zeroEDM are nearly indistinguishable. In contrast, at the extreme θ_L regions, this difference becomes apparent, signalling the presence of an EDM signal. Consequently, weights are distributed based on this difference, granting maximum weights to extreme θ_L values and zero weight to central θ_L values. This acts in accordance with the findings indicated by w_Λ and w_V .

This function is calculated by; $f(\theta_{L_i}^{EDM}, \lambda) - f(\theta_{L_i}^{zeroEDM}, \lambda)$, providing the weight for θ_L at a specific precession ϕ_a and energy λ shown in **figure 11(a)**. Within the appendix **figure 24** displays the shape for a specific precession, ϕ_a across all 500 λ slices, hence the solid appearance. There will be 28 other shapes similar to **figure 24** making up all the required weights. These weights were collated into a single array and applied to corresponding θ_L values as a function of:

$$w_S = \frac{|Signal|}{|Signal| + Background} = \frac{|\Delta(f(\theta_{L_i})|}{|\Delta(f(\theta_{L_i})| + f(\theta_{L_i}^{zeroEDM})}. \quad (8)$$

4 Discussion

Several other use cases of $\Delta(f(\theta_{L_i}))$ were trialled in the process, including:

$$w_S = |\text{signal}| = |\Delta(f(\theta_{L_i})|, \quad \text{and} \quad w_S = \frac{|\text{signal}|}{\sqrt{|\text{signal}| + \text{background}}} = \frac{|\Delta(f(\theta_{L_i})|}{\sqrt{|\Delta(f(\theta_{L_i})| + f(\theta_{L_i}^{\text{zeroEDM}})}}.$$

The first trialled shape does not provide the weighting as a function of the background events and hence larger signals dominate the shape and result in an incorrect weighting. Similarly the second trial, whilst it does consider the background, it overly emphasises the signal when the background is small and is therefore incorrect. The optimal shape, **equation 8** displays when a $|\text{signal}| \rightarrow 0$, the weight $w_S \rightarrow 0$ and when the $|\text{background}| \rightarrow 0$, the weight $w_S \rightarrow 1$. Meaning large signals are not overly emphasised.

With this considered, the weights are maximally allocated to regions that suggest an EDM. This is exhibited in **figure 11(b)**, where the most dense weights are placed in the extreme θ_L . Additionally the uncertainty for the Weighted Average, is dependant upon N, hence if the largest weights are allocated in the correct sensitive regions of θ_L . If the value of N is largest, the resultant uncertainty, σ_w is reduced. This uncertainty relative to measurement is therefore better than all previous statistics discussed.

Table 2 displays the optimised weight, when applied to the Weighted Average, provides a peak FOM, $W(w_S)_{FOM} = 9.9$ occurring at $\lambda \approx 0.5$. The ratio of performance against w_\square is always 1.2 times better across all energies. This achieves the aim of the paper, an effective measurement that characterises an EDM providing the most confidence in measuring a signal of EDM. **Figure 13** displays the results across 30 different energies:

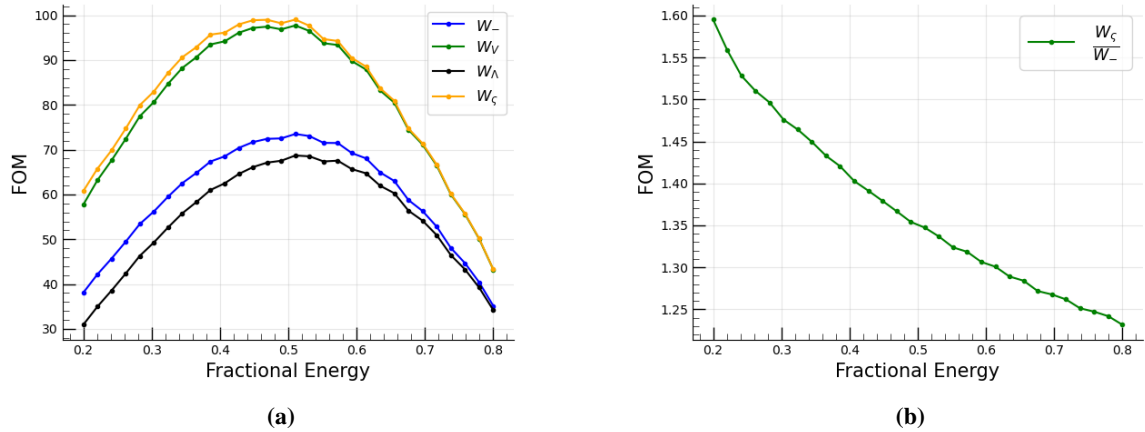


Figure 13: (a) Figure of Merit for 30 sliced energies ranging from $\lambda = 0.2 \rightarrow 0.8$. (b) ratio of the optimised Weighted Average against square Weighted Average for 30 different energies ranging from $\lambda = 0.2 \rightarrow 0.8$.

As shown in **figure 13(a)** and **table 2**, the optimised weight w_S produces the best possible result for the FOM. Only slightly beating w_V , but still performing the best. The square weight w_\square , provides an identical FOM to the Average Angle as expected. Finally w_A being the lowest.

Importantly, the FOM is almost identical when $\lambda \gtrapprox 0.7$, for w_S and w_V . This is shown in **figure 13(a)** and **table 2**. This is due to the shape of the optimised weight, **figure 11(b)** tending linear as the

momentum increases. As a result, they are the same shape at these values of λ . However the maximal EDM sensitivity occurs using the optimised weight at $\lambda \approx 0.5$ where $W(w_\zeta)_{FOM} = 9.9$ but the inverted weight $W(w_V)_{FOM} = 9.7$. This indicates that regardless of there performance in the region of $\lambda \gtrsim 0.7$ this is not of importance as it is not the maximal sensitivity.

Figure 13(b) demonstrates the ratio of performance across the energy spectrum when comparing the square weight w_\square to w_ζ . This displays an improvement on the current limit of the Average Angle (as $w_\square = \langle \theta_L \rangle$), where the FOM for the optimised Weighted Average is 1.4 times better than the Average Angle at the optimal energy, $\lambda \approx 0.5$.

4.3 The overall optimisation of the EDM sensitivity

Finally, **table 3** discusses the performance of the optimised Weighted Average as a resemblance of the entire project. The previous limit of the Asymmetry was beaten in its ability to characterise the EDM by the Average Angle, shown in **table 1** and **figure 12**. This provided the current limit of detection at $\langle \theta_L \rangle_{FOM} = 7.3$ for $\lambda \approx 0.5$, offering a 1.7 times greater sensitivity at this point compared to the Asymmetry. With **table 2**, a new improved limit through the optimised Weighted Average $W(\lambda)$, resulted in $W(w_\zeta)_{FOM} = 9.9$ occurring at $\lambda \approx 0.5$. This provides a 1.4 times improvement on the current limit of $\langle \theta_L \rangle$. In **table 3**, a comparison of the full improvement made throughout the project is clear with the optimised weight w_ζ yielding a FOM 2.3 times greater than the Asymmetry, at $\lambda \approx 0.5$. **Figure 14** displays the results visually:

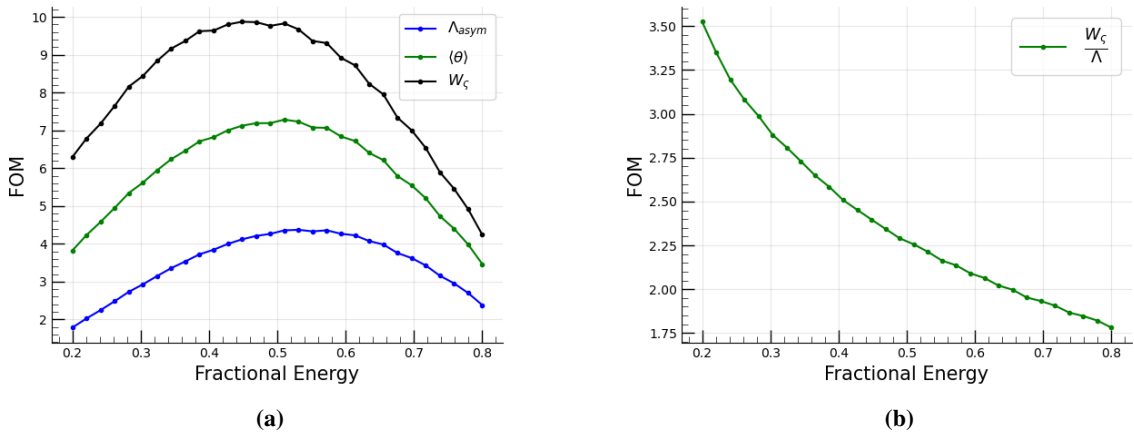


Figure 14: (a) Figure of Merit for 30 sliced energies ranging from $\lambda = 0.2 \rightarrow 0.8$. (b) ratio of the optimised Weighted Average against Asymmetry for 30 different energies ranging from $\lambda = 0.2 \rightarrow 0.8$.

The ultimate result illustrated in **figure 14(a)** demonstrates that the best EDM measurement is obtained with $W(w_\zeta)_{FOM} = 9.9$, at a fractional lab frame energy of $\lambda \approx 0.5$. This represents a substantial improvement above the current benchmark of $\langle \theta_L \rangle_{FOM} = 7.3$, which also surpassed the original boundary of $\Lambda_{FOM} = 4.3$. **Figure 14(b)** reveals that the optimised Weighted Average consistently outperforms the Asymmetry, by a factor of at least 1.8, with a peak improvement of 3.5 times at $\lambda \approx 0.2$.

The final parameters for greatest sensitivity are found at $\lambda \approx 0.5$, $\phi_a = \pm\frac{\pi}{2}$, when the weight w_S is applied to the Weighted Average $W(\lambda)$.

The superiority of the optimised Weighted average over the conventional Asymmetry, the Average Angle, and some trialled weighting functions has been established. While it is unlikely that another metric outperforms the optimised Weighted Average, statistical metrics, such as Skew and the Likelihood estimator, could be tested, but due to time constraints this was not performed at a high level. This suggests that, at present, the Weighted Average remains the most dependable and effective method for assessing the EDM. Given this, a more fitting progression of this work could involve emerging techniques such as Machine Learning and Monte Carlo simulations applied to the Weighted Average to further improve this statistic.

5 Conclusion

This project set out to enhance the sensitivity of muon EDM measurements within the g-2 experiment, by testing and evaluating statistical methods this project has improved the current capabilities of EDM signal extraction from muon decay data. This was accomplished by constructing a robust statistical framework that compared traditional metrics, such as the Asymmetry Λ and Average Angle $\langle \theta_L \rangle$ against the Weighted Average $W(\lambda)$, this demonstrated a clear advantage in adopting optimised statistical approaches. Applying the optimised weight w_S to the Weighted Average $W(\lambda)$, yields a significant increase in the FOM, with enhancements reaching up to 3.5 times the Asymmetry, Λ .

This result is not only statistically meaningful but has practical implications for improving the experimental sensitivity to an EDM signal, a crucial step in probing physics beyond the SM. Moreover, the developed methods are robust, scalable, and adaptable to future datasets, including those with improved statistics from ongoing or upcoming g-2 experiments. This project serves as a valuable contribution to the broader effort of particle physics, potentially aiding in the discovery of a non zero EDM for leptons. This project underscores the importance of data-driven techniques in particle physics. It should also be noted, in a practical setting the observable and useful ranges of θ_L will be limited in comparison to the data used in this project, hence further work should take this as a consideration to develop a more applicable tool to the field. Furthermore, due to time constraints and resource limitations, advanced techniques such as Machine Learning could not be explored in depth. This determination of a new maximised detection limit provides a sufficient statistic for future analysis of the muon EDM. If an EDM of order $10^{-30} ecm$ or greater were to be detected this would strongly imply physics beyond the SM such as the matter-antimatter asymmetry. Currently the limit of CP violation in the universe is exceedingly small to explain the asymmetry. New physics suggesting CP violation processes through a measurable EDM would aid in this explanation. This project has complemented modern particle physics beyond its current limit through a synergy of computation and statistics, revealing a new limit of EDM detection though the optimised Weighted Average. Ultimatley, under the same practical setup utilised at Fermilab, this statistic proves to be more efficient, necessitating a smaller number of decay events to ascertain the presence of a permanent EDM within leptons.

References

- [1] S. Navas et al. Muon properties – 2024 review of particle physics.
<https://pdg.lbl.gov/2024/listings/rpp2024-list-muon.pdf>, 2024. Date of Acess: 11:04:2024.
- [2] Seth H. Neddermeyer and Carl D. Anderson. Note on the nature of cosmic-ray particles.
https://spark.liceodesio.edu.it/pluginfile.php/5830/mod_resource/content/1/muon_discovery.pdf, 1937. Date of Acess: 11:04:2024.
- [3] Fermilab Muon g 2 Collaboration. Measurement of the positive muon anomalous magnetic moment to 0.46 ppm.
<https://doi.org/10.1103/PhysRevLett.126.141801>, 2021. Date of Acess: 11:10:2024.
- [4] Saïda Guellati-Khelifa. Searching for new physics with the electron’s magnetic moment. *Physics*, 16:22, 2023. Accessed: 2025-04-17.
- [5] J. M. Cassels. Pion and muon decay.
<https://royalsocietypublishing.org/doi/10.1098/rspa.1958.0153>, 1958. Date of Acess: 11:10:2024.
- [6] Richard L. Garwin, Leon M. Lederman, and Marcel Weinrich. Observations of the failure of conservation of parity and charge conjugation in meson decays: The magnetic moment of the free muon, 1957. Accessed: 2025-04-04.
- [7] ATLAS Collaboration. Observation of a new particle in the search for the standard model higgs boson with the atlas detector at the lhc.
<https://doi.org/10.1016/j.physletb.2012.08.020>, 2012. Date of Acess: 11:12:2024.
- [8] CMS Collaboration. Observation of a new boson at a mass of 125 gev with the cms experiment at the lhc.
<https://doi.org/10.1016/j.physletb.2012.08.021>, 2012. Date of Acess: 11:12:2024.
- [9] G. W. Bennett et al. Final report of the e821 muon anomalous magnetic moment measurement at bnl.
<https://doi.org/10.1103/PhysRevD.73.072003>, 2021. Date of Access: 11:12:2024.
- [10] G.W. Bennett et al. An improved limit on the muon electric dipole moment.
<http://arxiv.org/abs/0811.1207v2>, 2009. Date of Acess: 11:14:2024.
- [11] Nathan B. Xavier R. Bufalo. On the presence of electric dipole and toroidal moments in non-hermitian qed.
<https://www.sciencedirect.com/science/article/pii/S0370269324007251>, 2025. Date of Access: 04:04:2025.
- [12] T. Aoyama and et al. The anomalous magnetic moment of the muon in the standard model.
<https://www.sciencedirect.com/science/article/pii/S0370157320302556>, 2020. Accessed: 2025-04-04.

References

- [13] W. M. Yao et al. Review of particle physics. *Journal of Physics G: Nuclear and Particle Physics*, 33:1–1232, 2006. Section: CP Violation in Leptonic Decays.
- [14] I.B. Khriplovich and S.K. Lamoreaux. *CP Violation Without Strangeness: Electric Dipole Moments of Particles, Atoms, and Molecules*. Springer, 1997. Springer-Verlag, Berlin Heidelberg.
- [15] Andrei D. Sakharov. Violation of cp invariance, c asymmetry, and baryon asymmetry of the universe.
http://jetpletters.ru/ps/1643/article_25089.pdf, 1967. Date of Access: 11:14:2024.

Appendix

Uncertainty Analysis

$$\Delta I_u = \sqrt{N_u} \quad (9)$$

$$\Delta I_d = \sqrt{N_d} \quad (10)$$

$$\Delta I = \sqrt{(\delta I_u)^2 + (\delta I_d)^2} \quad (11)$$

$$\Delta \Lambda = |\Lambda| \sqrt{\left(\frac{\delta I}{N_u - N_d} \right)^2 + \left(\frac{\delta I}{N_u + N_d} \right)^2} \quad (12)$$

$$\sigma_{\theta_{L_i}}(\lambda) = \sqrt{\frac{1}{\sum f(\theta_{L_i}, \lambda)} \sum f(\theta_{L_i}, \lambda) \cdot (\theta_{L_i} - \langle \theta_{L_i} \rangle)^2} \quad (13)$$

$$\Delta \langle \theta_{L_i} \rangle = \frac{\sigma_{\theta_{L_i}}}{\sqrt{f(\theta_{L_i}, \lambda) - 1}} \quad (14)$$

$$n_{\text{eff}} = \frac{(\sum f(\theta_{L_i}, \lambda) \cdot w)^2}{\sum f(\theta_{L_i}, \lambda) \cdot w^2} \quad (15)$$

$$\sigma_w^2 = \frac{\sum w \cdot f(\theta_{L_i}, \lambda) \cdot (\theta_L - W(\lambda))^2}{\sum f(\theta_{L_i}, \lambda) \cdot w} \times \frac{n_{\text{eff}}}{n_{\text{eff}} - 1} \quad (16)$$

$$\sigma_w = \frac{\sqrt{\sigma_w^2}}{\sqrt{n_{\text{eff}}}} \quad (17)$$

Plots

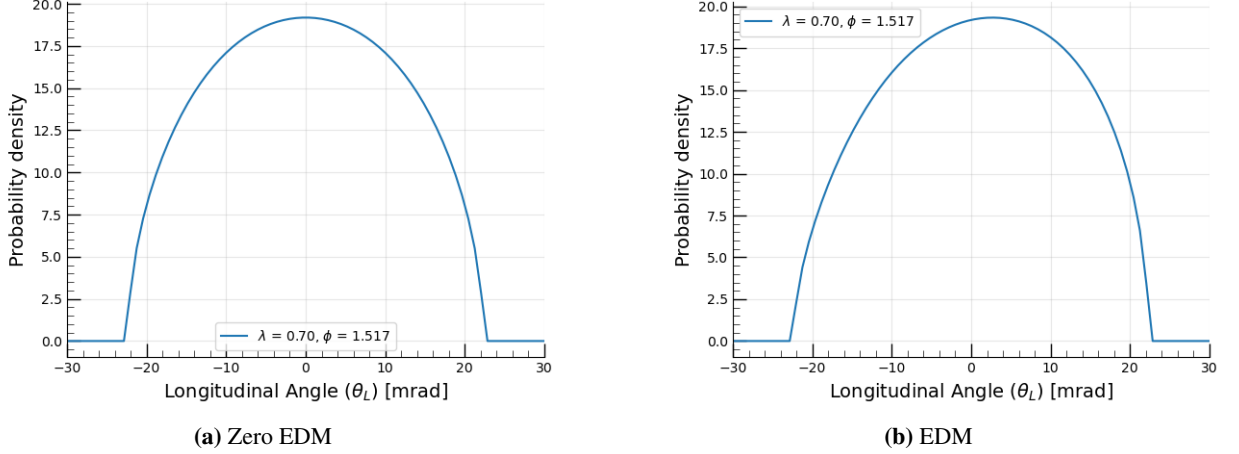


Figure 15: Comparison of singular Probability Density plots. (a) with zeroEDM and (b) with EDM. The chosen lab frame decay energy $\lambda = 0.7$ and the precession index $\phi_a = 1.950\text{rads}$. There is no specific reason for the slicing to be of these values, a random choice for demonstration.

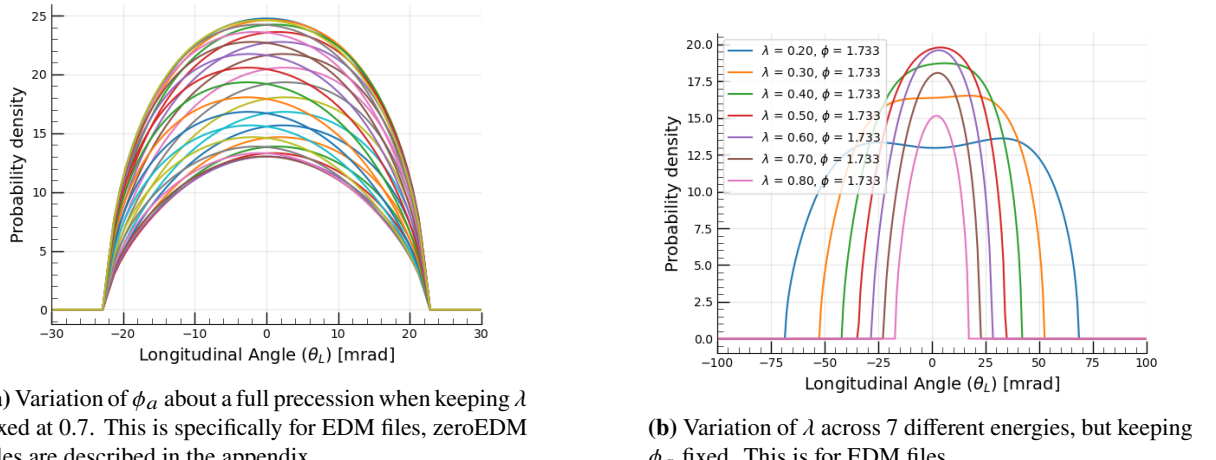
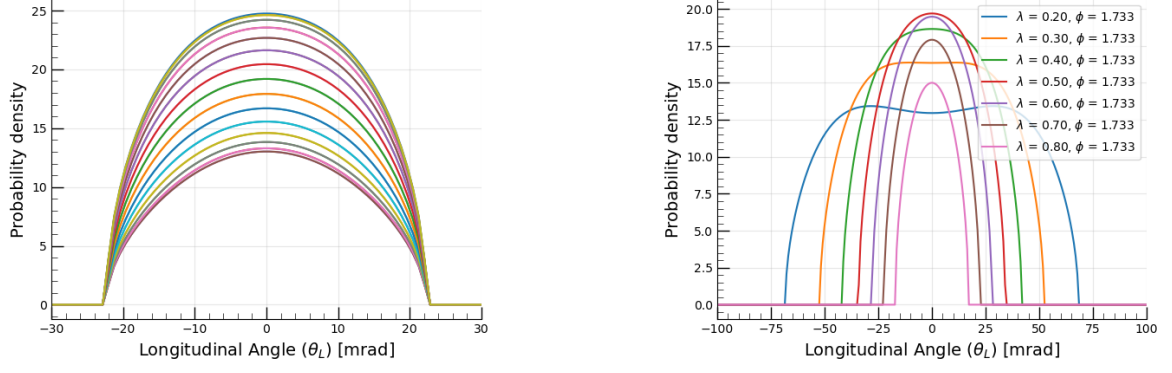


Figure 16: A comparison between the results of varying ϕ_a and λ whilst keeping each other fixed.



(a) Variation of ϕ_a about a full precession when keeping λ fixed at 0.7. This is specifically for zeroEDM files

(b) Variation of λ across 7 different energies, but keeping ϕ_a fixed. This is for zeroEDM files.

Figure 17: A comparison between the results of varying ϕ_a and λ whilst keeping each other fixed.

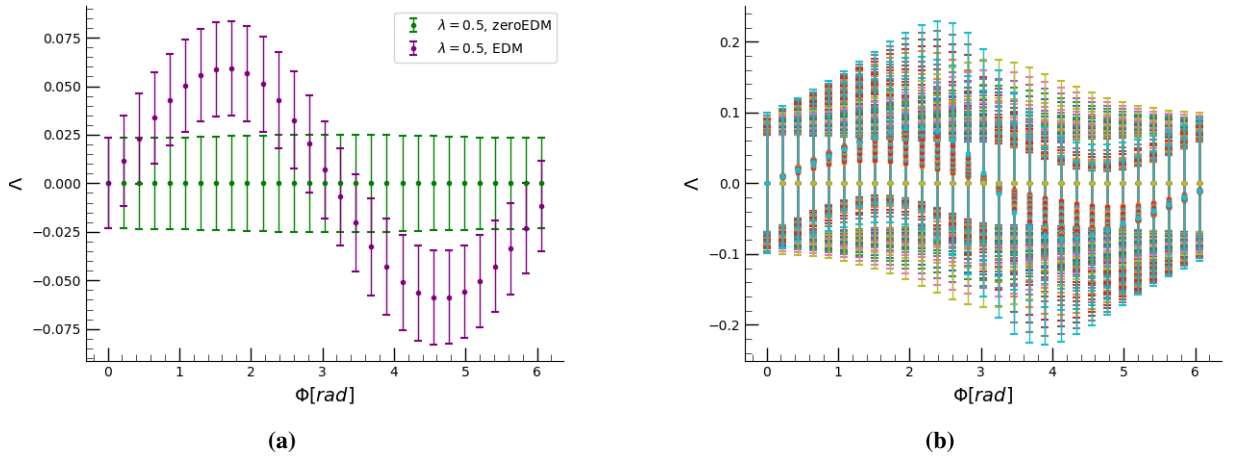


Figure 18: (a) The Asymmetry Λ measured for each 29 files, both EDM and zeroEDM at the energy of $\lambda = 0.5$.
 (b) The Asymmetry, Λ , calculated for a full precession series, ϕ_a , and iterated over the entire energy spectrum, λ for 30 slices.

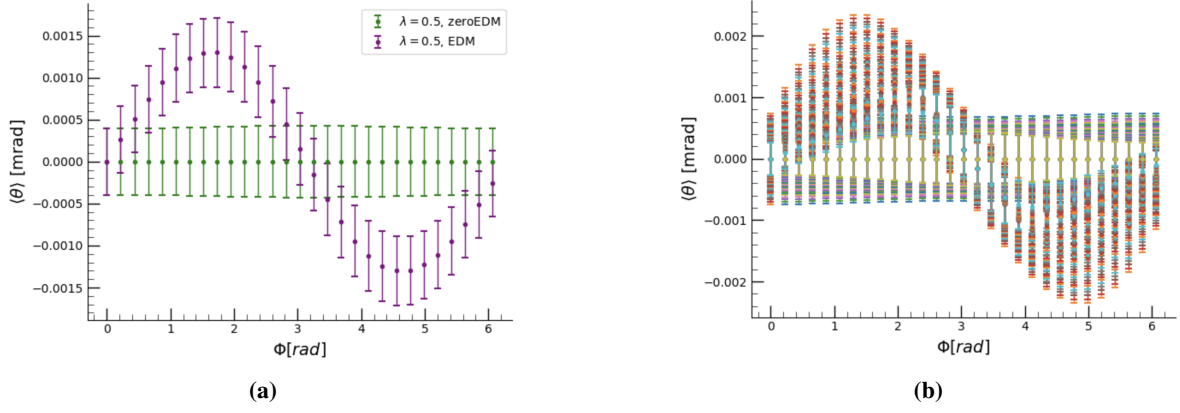


Figure 19: (a) The Average Angle $\langle \theta_L \rangle$ measured for each 29 files, both EDM and zeroEDM at the energy of $\lambda = 0.5$. (b) The Average Angle, $\langle \theta_L \rangle$, calculated for a full precession series, ϕ_a and iterated 3 the entire energy spectrum, λ for 30 slices.

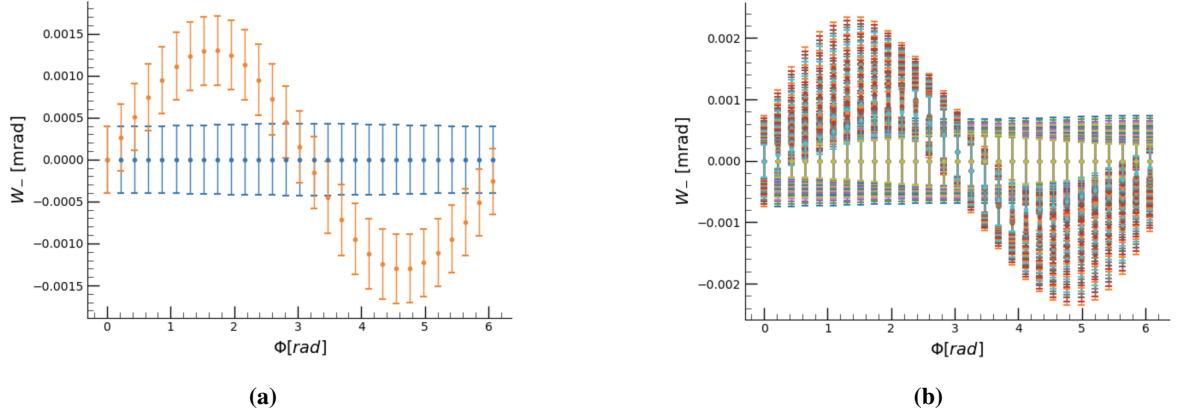


Figure 20: (a) The Weighted Average using the square weight, w_{\square} , measured for each 29 files, both EDM and zeroEDM at the energy of $\lambda = 0.5$. (b) The Weighted Average, calculated for a full precession series, ϕ_a and iterated over the entire energy spectrum, λ for 30 slices.

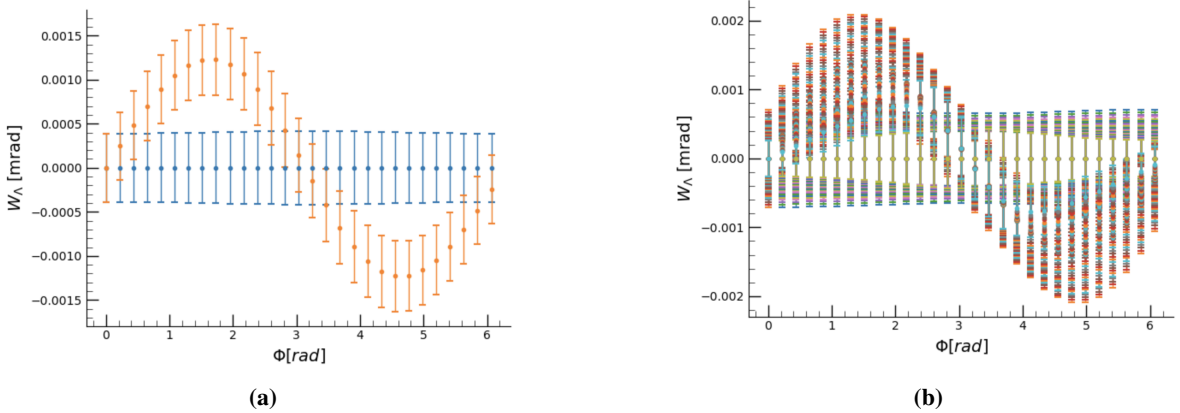


Figure 21: (a) The Weighted Average using the triangular weight, w_Λ , measured for each 29 files, both EDM and zeroEDM at the energy of $\lambda = 0.5$. (b) The Weighted Average, calculated for a full precession series, ϕ_a and iterated over the entire energy spectrum, λ for 30 slices.

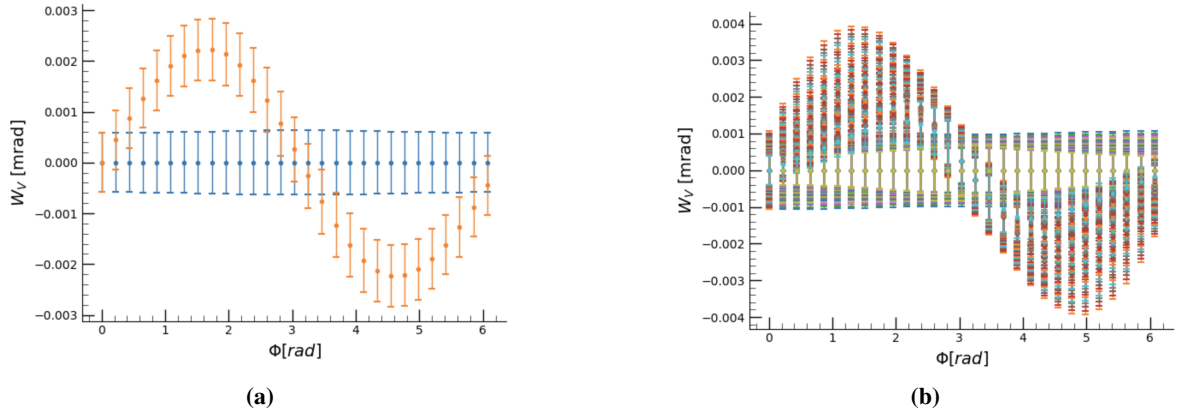


Figure 22: (a) The Weighted Average using the inverted w_V , measured for each 29 files, both EDM and zeroEDM at the energy of $\lambda = 0.5$. (b) The Weighted Average, calculated for a full precession series, ϕ_a and iterated over the entire energy spectrum, λ for 30 slices.

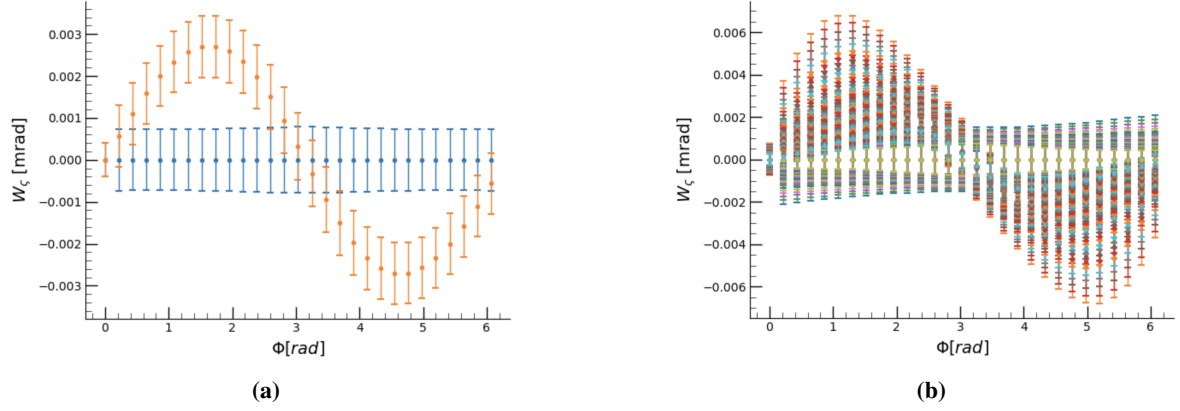


Figure 23: (a) The Weighted Average using the optimised weight, w_ζ , measured for each 29 files, both EDM and zeroEDM at the energy of $\lambda = 0.5$. (b) The Weighted Average, calculated for a full precession series, ϕ_a and iterated over the entire energy spectrum, λ for 30 slices.

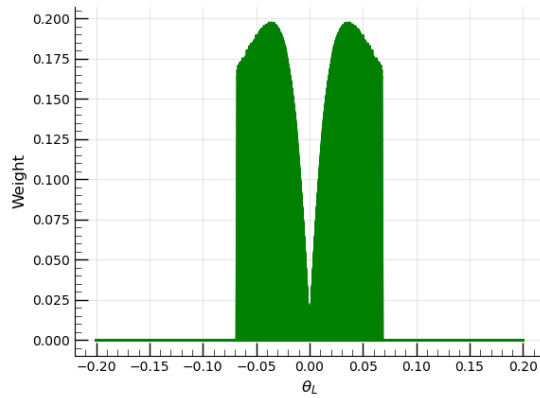


Figure 24: Collection of the optimised weight across all λ , where **figure 11(a)** displays a singular sliced weight. This is for precession index = 7

```

z_diff_array = []
#list of all .pkl files in the folder
files = [f for f in os.listdir(inFolder) if f.endswith('.pkl')]
#Files with and without EDM
filesEDM = [f for f in files if 'withEDM' in f]
filesNoEDM = [f for f in files if 'withEDM' not in f]
#combined plots
combined_results = []
filesEDM.sort()
filesNoEDM.sort()
for edm_file in filesEDM:
    # Extract phase index from the EDM file name
    phaseIndex = int(edm_file.split('_')[1].split('.')[0])
    #print(phaseIndex)
    # Load Z1 from the EDM file
    with open(os.path.join(inFolder, edm_file), "rb") as f:
        X1, Y1, Z1 = pickle.load(f) # Z1 from EDM files
    # Loop through each non-EDM file to find a corresponding Z2
    for no_edm_file in filesNoEDM:
        # Extract phase index from the non-EDM file name
        no_edm_phaseIndex = int(no_edm_file.split('_')[1].split('.')[0])
        # Ensure we are comparing the same phase
        if phaseIndex == no_edm_phaseIndex:
            # Load Z2 from the non-EDM file
            with open(os.path.join(inFolder, no_edm_file), "rb") as f:
                X2, Y2, Z2 = pickle.load(f) # Z2 from non-EDM files
            # Ensure X and Y are the same for both datasets
            if np.array_equal(X1, X2) and np.array_equal(Y1, Y2):
                # Calculate the difference Z1 - Z2
                Z_diff = (Z2 - Z1)
                Z_diff = np.divide(np.fabs(Z_diff), np.fabs(Z_diff) + Z2, out=np.zeros_like(Z_diff), where=Z1!=0)
                # Store the Z_diff in the array
                z_diff_array.append(Z_diff)
                # Store results for later processing or plotting
                combined_results.append((phaseIndex, Z_diff, X1, Y1))
            else:
                print(f"Phase {phaseIndex} data shapes do not match. Skipping...")
            break # Exit the inner loop after finding the corresponding file
z_diff_array = np.array(z_diff_array)
soverb = z_diff_array
for i, weightmap in enumerate(soverb):
    tol = 1E-4
    tmp = np.max(weightmap)
    if tmp < tol:
        print("For index", i, "max is", tmp, "setting to uniform")
        soverb[i] = np.ones_like(weightmap)
wz_ = (np.fabs(soverb))

```

Figure 25: Code to reproduce the optimised weighting function using the available .pkl files

```

def weight_0(theta, l):
    M = 1.0
    w = M * np.ones_like(theta)

    slope = M/theta[:,0][-1]
    w_left = np.where(theta < 0, -1*slope * theta + 0, 0)
    w_right = np.where(theta > 0, 1*slope * theta + 0, 0)

    w_lr = w_left + w_right
    return w

def weight_1(theta, l):
    M = 1.0
    w = M * np.ones_like(theta)

    slope = M/theta[:,0][-1]
    w_left = np.where(theta < 0, -1*slope * theta + 0, 0)
    w_right = np.where(theta > 0, 1*slope * theta + 0, 0)

    w_lr = w_left + w_right
    w_lr[theta == 0] = 0

    return w_lr

def weight_2(theta, l):
    M = 1.0
    w = M * np.ones_like(theta)      slope = M/theta[:,0][-1]
    w_left = np.where(theta < 0, slope * theta + M, 0)
    w_right = np.where(theta > 0, -1*slope * theta + M, 0)
    w_lr = w_left + w_right
    return w_lr

```

Figure 26: Code to reproduce the weighting functions $w_{\square} = w0$, $w_{\Delta} = w2$, $w_V = w1$

```

w = wz_[phaseIndex, :, lindex]
n = np.sum(z*w)
neff = np.sum(z*w)**2 / np.sum(z*w**2)

dx = theta[1] - theta[0]
w_average = np.sum(theta * w * z) / n
wvar = np.sum(w * z * ((theta - w_average)**2)) / n * (neff / (neff-1))
w_std = np.sqrt(wvar) / np.sqrt(neff)

```

Figure 27: Application of a defined weight into the Weighted Average calculation

```

def integrate(theta, z):

    I_left = (theta >= -np.pi) & (theta <= 0)
    I_right = (theta > 0) & (theta <= np.pi)

    dx = theta[1] - theta[0]

    N_d = np.trapz(z[I_left], theta[I_left], dx = dx)
    N_u = np.trapz(z[I_right], theta[I_right], dx = dx)

    integrated_result = N_d + N_u
    return N_d, N_u, integrated_result


def int_err(N_d, N_u):
    I_left_err = np.sqrt(N_d)
    I_right_err = np.sqrt(N_u)

    return I_left_err, I_right_err


def aysm(N_d, N_u):

    asymmetry = (N_u - N_d) / (N_u + N_d)
    return asymmetry

```

Figure 28: Asymmetry Function Code

```

avg_theta = np.sum(theta*z) / np.sum(z)
variance = np.sum( z*((theta - avg_theta)**2)) / np.sum(z)
std_dev = np.sqrt(variance)
mean_err = std_dev/(np.sqrt(np.sum(z) - 1))

```

Figure 29: Code to reproduce the average angle